US Contributions to the Athena Wide Field Imager

David N. Burrows[a], Steve Allen[b,g], Marshall Bautz[c], Esra Bulbul[d], Tanmoy Chattopadhyay[b], Julia Erdley[a], Abraham D. Falcone[a], Catherine E. Grant[c], Sven Herrmann[b,f], Ann Hornschemeier[e], Doug Kelly[a], Jamie Kennea[a], Ralph Kraft[d], Beverly LaMarr[c], Adam Mantz[b], Eric D. Miller[c], R. Glenn Morris[b,g], Paul Nulsen[d], Pragati Pradhan[a], Neven Vulic[e,h], Dan Wilkins[b], and Michael E. Zugger[a]

[a]Department of Astronomy & Astrophysics, The Pennsylvania State University, 525 Davey Lab, University Park, PA, USA
[b]Department of Physics, Stanford University, 382 Via Pueblo Mall, Stanford CA 94305
[c]MIT Kavli Institute for Astrophysics and Space Research, Cambridge, MA
[d]Smithsonian Astrophysical Observatory, Cambridge, MA
[e]NASA Goddard Space Flight Center, Greenbelt, MD
[f]Brookhaven National Laboratory, Upton, New York 11973
[g]SLAC National Accelerator Laboratory, 2575 Sand Hill Road, Menlo Park, CA 94025
[h]University of Maryland, College Park, MD

ABSTRACT

The world's premier X-ray astronomical observatories, *Chandra* and *XMM-Newton*, have been operating for about 20 years. The next flagship X-ray observatory launched will be ESA's *Athena* mission. We discuss planned US contributions to the *Athena* Wide Field Imager instrument, which encompass transient source detection, background characterization and reduction, and detector electronics design and testing, in addition to scientific contributions.

Keywords: X-ray astronomy, Athena, Wide Field Imager

1. INTRODUCTION

The *Athena* Wide Field Imager (WFI) instrument has been discussed in many SPIE publications, and we refer the interested reader to those publications for details of the instrument design.[1–11] Our team will provide contributions to the WFI instrument to enhance its scientific value, and we describe the current status of these contributions here. They come in three broad categories: detection of serendipitous X-ray transients in the WFI field of view, improving the knowledge of and (if possible) reducing the instrumental background in order to permit study of faint diffuse objects like cluster outskirts, and contributions to the design and testing of the front-end detector electronics.

2. TRANSIENT SOURCE DETECTION

We are in an era of time domain astronomy. Transient and variable sources are particularly dominant in the high energy portion of the electromagnetic spectrum, which sees emission from black holes of all masses as well as from cataclysmic explosions like supernovae and gamma-ray bursts. With its wide field of view ($40' \times 40'$) and excellent sensitivity, the WFI will detect thousands of variable or transient sources daily. A few examples include supernova shock breakouts, first discovered by the Swift X-ray Telescope (Fig. 1),[12] tidal disruption events (TDEs), off-axis GRBs, and blazar/AGN high states. Of particular interest are unexplained source classes such as the Fast X-ray Transients found in Chandra archival data and Fast Radio Bursts. Rapid localization of such objects could be crucial in finding counterparts at other wavelengths (or with other messengers) and thereby elucidating their nature.

UV, X-Ray, and Gamma-Ray Space Instrumentation for Astronomy XXI, edited by Oswald H. Siegmund, Proc. of SPIE
Vol. 11118, 111180Z · © 2019 SPIE · CCC code: 0277-786X/19/$21 · doi: 10.1117/12.2528532

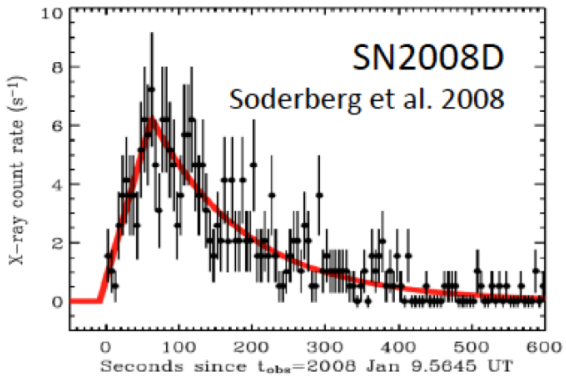

Figure 1. *Swift* XRT light curve of the supernova shock breakout of SN2008D.[12]

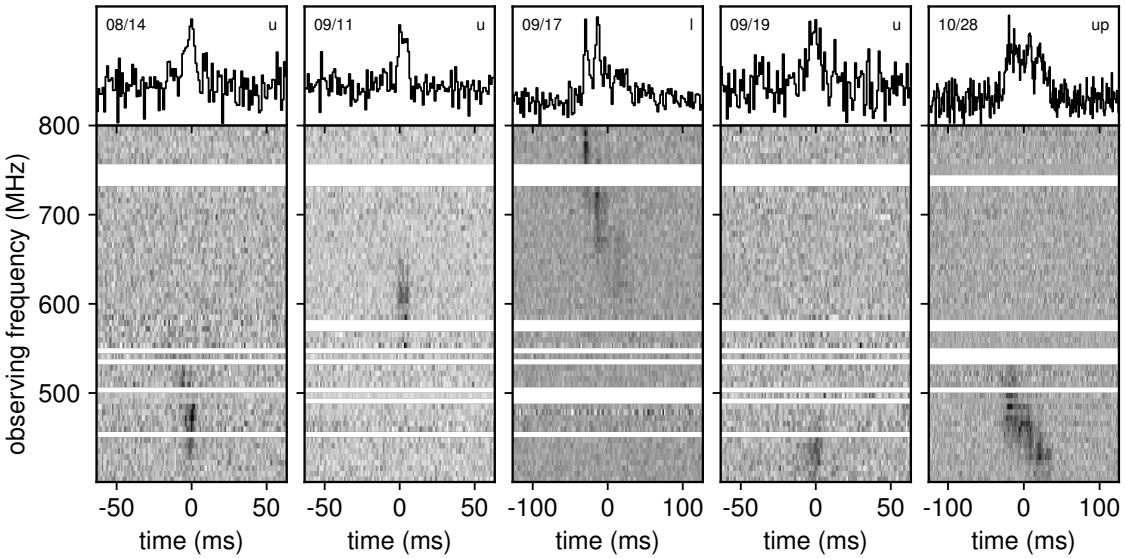

Figure 2. The repeating Fast Radio Burst FRB180814.J0422+73.[13]

To get a feeling for the scope of the variable source population we can look to a study of serendipitous variable X-ray sources in 8 years of observations by the *Swift* XRT,[14] which found $\sim 28,000$ variable sources, or roughly 10 new variable sources per day (Fig. 3). *Swift* has an observing efficiency of about 79%, an effective area of about 120 cm^2, and a roughly circular field of view of 23.6 arcminutes diameter. The WFI, by contrast, will have roughly 100× the collecting area and $\sim$ 3× the field of view of the XRT. A simple (perhaps simplistic) extrapolation suggests that the WFI will detect hundreds to thousands of variable sources per day (assuming a $\log N - \log S$ slope of $-3/2$ and scaling by the instrument FOV). We expect that the mission will be in real-time contact with the ground for 4 hours per day (16% of the time), potentially allowing rapid alerts of any transients discovered during ground passes.

We have developed a simple prototype algorithm for rapid transient source detection.[15] This algorithm (referred as the Transient Analysis Module, or TAM) was originally intended to be implemented on-board for real-time transient detection on the instrument, but could also serve as a ground-based transient source detection algorithm. A flow diagram for the prototype algorithm is shown in Fig. 4. The TAM algorithm identifies sources in the field of view on a variety of time scales and determines whether or not they are in the on-board catalog,

Further author information: (Send correspondence to D. N. Burrows)
D. N. Burrows: E-mail: dxb15@psu.edu, Telephone: +1 (814) 863-2466

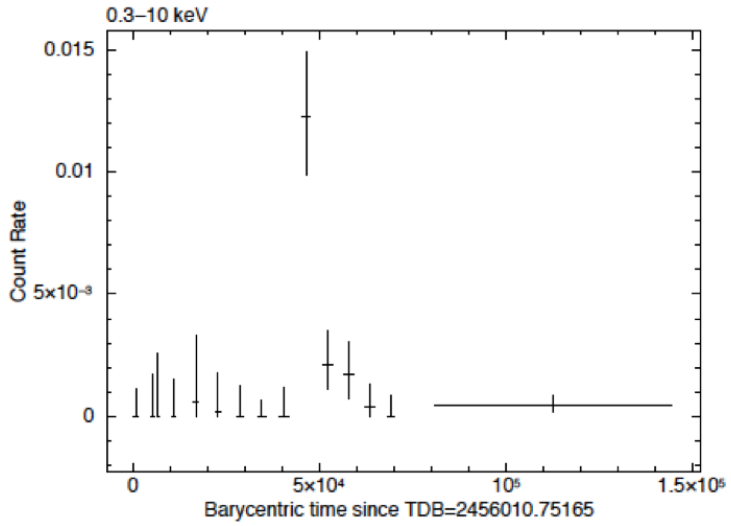

Figure 3. 1SXPS J192427.2+240925, a serendipitous transient source found in the *Swift* XRT archive. The *Swift* XRT found an average of about 10 such sources per day over the first 8 years of observations,[14] which were dominated by GRB observations distributed randomly on the sky.

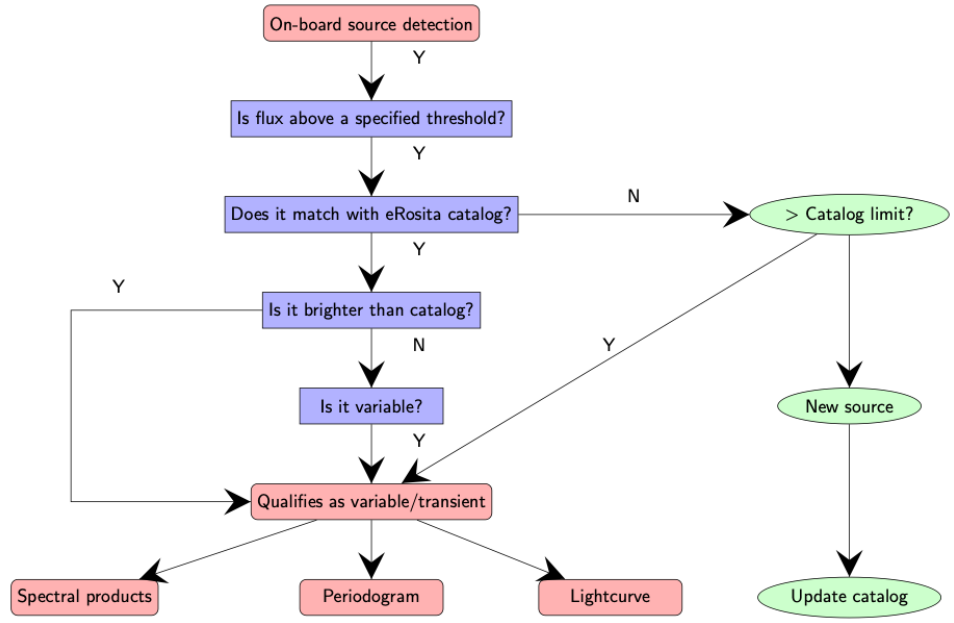

Figure 4. Flow chart for the prototype WFI transient detection algorithm.[15]

which we expect to be based on the eROSITA source catalog. If a source is found to be new (above the catalog limit but not in the catalog) or variable (in the catalog but significantly above the catalog flux), then we will produce quick-look data products including the source position, light curves in several energy bands, hardness ratios, and the results of a periodicity search.

We tested the prototype TAM algorithm on data sets constructed with the SIXTE X-ray simulation tool.[16] Data sets were created in SIXTE using the Chandra Deep Field South (CDFS) sources included as part of the SIXTE tool. We added a variety of artificial variable sources designed to test the robustness of our algorithm at recovering weak sources at various count rates and with different types of light curves, including fast turn-ons

and turn-offs. We also included several strongly variable sources using *XMM-Newton* light curves and spectral properties. Overall, our algorithm was quite successful at identifying and correctly characterizing these sources, with the exception of periodic sources with periods below the chosen sampling frequency of 100-second binning.* A more complete algorithm would mitigate this by searching for variability on a variety of time scales. We found that we met all of the imposed requirements with the exception of real-time, on-board source identification during slews, where the calculation time of exposure maps exceeded the time it took a source to cross the field of view (about 10 s). We identified several possible mitigations for this problem to allow on-board source detection during slews, including pre-calculation of exposure maps for slews, or ground post-processing of those exposure maps.

Sample data products produced by the prototype TAM algorithm are shown in Fig. 5 for the source LMC X-4, for which XMM data were injected into the SIXTE simulation with an arbitrary flux normalization (we did not correct for the difference in collecting area). These include a light curve over the instrument bandpass, hardness

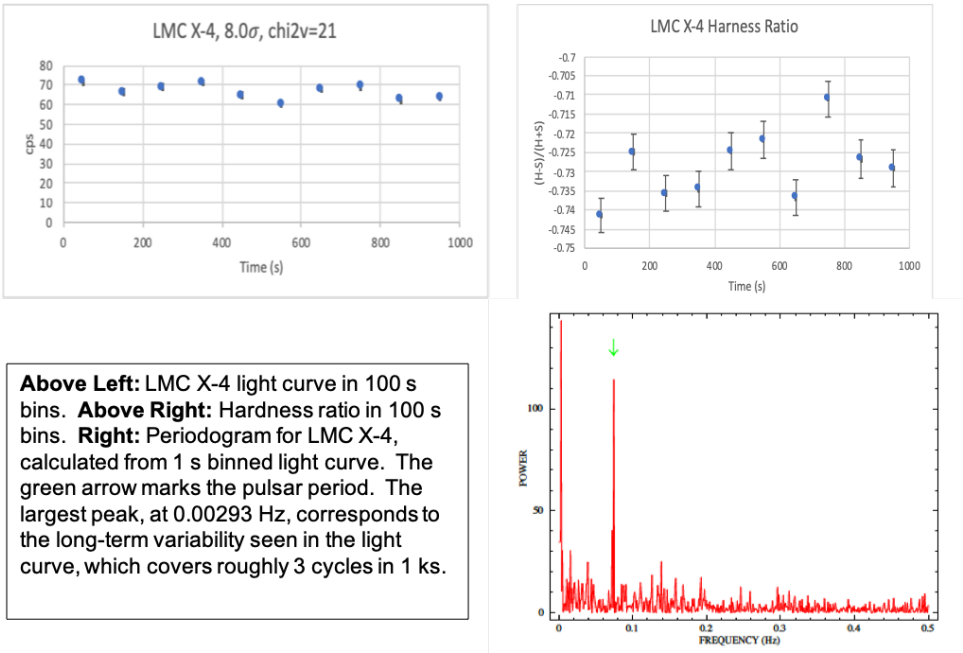

Above Left: LMC X-4 light curve in 100 s bins. **Above Right:** Hardness ratio in 100 s bins. **Right:** Periodogram for LMC X-4, calculated from 1 s binned light curve. The green arrow marks the pulsar period. The largest peak, at 0.00293 Hz, corresponds to the long-term variability seen in the light curve, which covers roughly 3 cycles in 1 ks.

Figure 5. Sample output products from the prototype WFI transient detection algorithm for a simulated observation of LMC X-4 with arbitrary source flux normalization.[15]

ratios as a function of time during the observation, and a periodogram, which was successful in recovering the period of the X-ray pulsar. We expect to use more sophisticated processing techniques in the final algorithm; these were intended as a demonstration of capabilities and to estimate the timing requirements of the data processing.

3. BACKGROUND REDUCTION AND CHARACTERIZATION

One of the key science goals (SG1.3) of the *Athena* mission is to identify non-gravitational cluster heating processes.† To quote the proposal, "This requires X-ray surface brightness and gas temperature measurements down to the background-dominated regime." This drives the requirement on the WFI background level in the 2–7 keV band.

*In the case of LMC X-4 (Fig. 5) the source variability seen in the light curve was detected on 100-s sampling, while the pulsar period was found found by a periodogram with 1-s sampling.

†See the *Athena* mission proposal to ESA, available at https://www.cosmos.esa.int/documents/400752/400864/Athena+Mission+Proposal/18b4a058-5d43-4065-b135-7fe651307c46.

Models of the expected WFI background, derived from detailed GEANT4 simulations, currently predict that this requirement will not be met without additional processing.[17] We have been studying both the GEANT4 simulations by the Open University and by MPE, and in-flight data from the *XMM-Newton* EPIC pn CCD instrument, which has similar pixel size and depletion depth to the WFI DEPFETs, in order to investigate whether the non-X-ray background can be reduced and/or to improve its characterization.

The GEANT4 simulations provided by Jonathan Keelan of the Open University contain 1.33×10^8 Galactic cosmic ray protons drawn from the CREME96 standard spectral model for solar minimum[18] and generated on a 70-cm radius sphere surrounding the WFI mass model. These simulations used the simplified E0015261 WFI mass model, from July 2017, which includes the camera, proton shield, filter wheel, and baffle, but not the graded-Z shield. These simulations are valuable because they provide a detailed physics-based simulation of the interaction of primary cosmic rays with the spacecraft and instrument. We know that all the events produced in the DEPFET detectors by these simulations are related to cosmic rays and are therefore background events. Figure 6 shows a mosaic of some of the particle tracks produced in these simulations. In addition to linear tracks

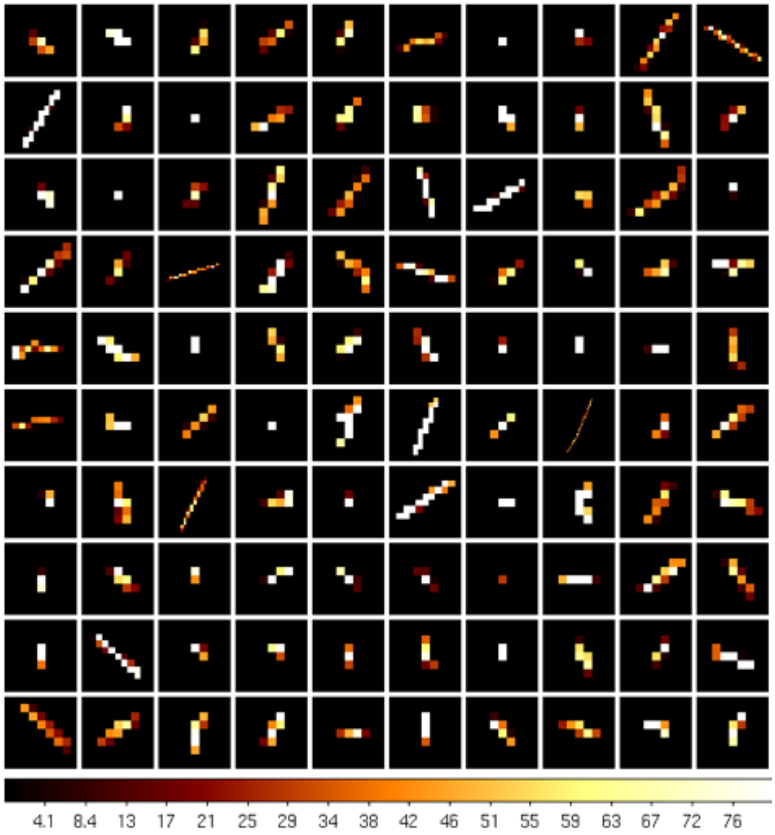

Figure 6. A sample of particle tracks produced by the GEANT4 simulations of cosmic ray interactions with the WFI instrument from Jonathan Keelan of the Open University. The colorscale shows energy in keV.

that are clearly produced by particles traversing the detector, there are events that consist of single pixels or of a few adjacent pixels that are similar to the events produced by cosmic X-rays. Since the WFI uses simple morphological tests to distinguish X-rays from background events, these are considered "valid" events by the event recognition algorithm and account for the bulk of the non-focussed background.

An analysis of *XMM-Newton* EPIC pn CCD data taken in small window mode with the filter wheel in the closed position confirms this conclusion.[19] Although the *XMM-Newton* EPIC instrument is not identical to the WFI, the detector has similar characteristics, with a pixel size of $150 \times 150\mu$m (*cf* $130 \times 130\mu$m for the WFI DEPFETs) and a depletion depth of 280μm (*cf* 450μm for the WFI), and the 64×64 pixel frames are read

out every 5.67 ms (*cf* 5 ms for the WFI). Since the filter wheel is closed for these observations, there are no cosmic X-rays striking the detector, so every event is an instrumental background event. Examining the count rate of valid background events in frames without any particle tracks from 1 Ms of observations taken in this configuration since 2007, we find a strong anticorrelation with the solar cycle, indicating that these "valid" events are actually associated with Galactic cosmic rays, which are modulated by the solar cycle (Fig. 7).

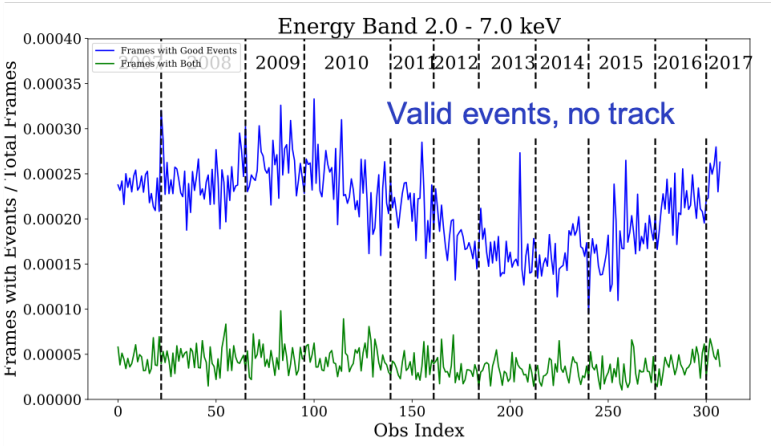

Figure 7. The fraction of frames with "valid" events found in 1 Ms of *XMM-Newton* EPIC pn CCD data taken since 2007 in small window mode (64×64 pixel window) with the filter wheel shut.[19] The blue curve shows events that are not accompanied by particle track, while the green curve shows events that *are* accompanied by a particle track. Solar minima occurred in 2009 and 2019. An anticorrelation with the 11-year solar cycle is present in both data sets, but is obvious in the blue curve because of the higher statistics.

The WFI Background Working Group has suggested that the WFI background can be reduced by "Self-Anticoincidence" (SAC); namely by rejecting all or portions of data frames that contain a particle track. We use the GEANT4 data simulations to explore the efficacy of this approach.

Working directly with the GEANT4 data, we can sort the frames into 4 types:

- Case A: Particle tracks, no valid events
- Case B: Valid events, no particle tracks
- Case C: Particle tracks and valid events
- Case D: no charge deposited by the primary particle (we do not consider this case further)

The particle interaction statistics for the GEANT4 data are summarized in Table 1. Nearly all of the particles that produce detected signal consist of Case A frames, which contain a particle track but no valid events. These frames account for 97.3% of the primary particles that interact in the detector, but do not contribute to the background. For the remaining primaries that produce signal, 65% of them (the Case B primaries) produce valid events without particle tracks. Because of the lack of detected particle tracks, these events cannot be vetoed using the SAC technique. Only the 35% of cosmic ray-produced valid events from Case C primaries could be "vetoed" by SAC. This is sufficient to reduce the 2–7 keV unrejected background below the requirement of 5×10^{-3} cm^{-2} s^{-1} keV^{-1},[17] however a large amount of signal would be lost by also vetoing in Case A frames that don't contain valid background events.

We further investigated the efficacy of self-anticoincidence in the Case C data.[20] We calculate the distance, r_e, between each valid Case C event and the nearest particle track, as shown in Fig. 8. We then calculated (from the Case C GEANT4 data) the cumulative probability of finding a valid event within r_e of a particle track. This tells you how effective a given size of exclusion region around each particle track is in reducing the unfocused

Table 1. GEANT4 event statistics for single particle primaries

Case A	
# of primaries producing **particle track** but **no valid event**	909,823 (97.3%)
Fraction of 2–7 keV background	0%
# of particle tracks per primary	1.12
Case B	
# of primaries producing **valid event** but **no particle track**	16,842 (1.8%)
Fraction of 2–7 keV background	65%
# of particle tracks per primary	0
Case C	
# of primaries producing **particle track and valid event**	8,839 (0.9%)
Fraction of 2–7 keV background	35%
# of particle tracks per primary	1.89

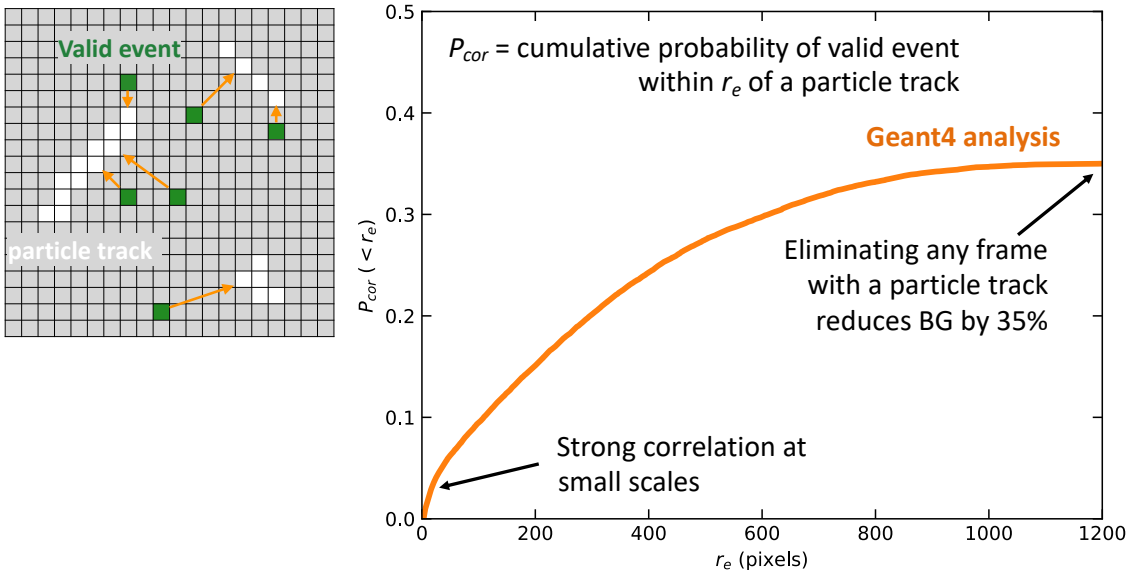

Figure 8. *Left:* diagram showing how the distance, r_e, from a valid event (green pixel) to the nearest particle track (which pixels) is calculated. *Right:* the cumulative probability of finding a valid event within a distance r_e of a particle track.

background from these interactions. There is a strong correlation at small values of r_e, but the curve flattens out at large r_e and reaches a peak value of 35% when r_e exceeds the full WFI FOV size (note that the four WFI detectors are each 512×512 pixels in size, so that r_e cannot exceed 724 pixels unless data are correlated between detectors).

The "rolling shutter" readout mode of the DEPFET detectors complicates the attempt to perform SAC, since the exposure time interval for each row is slightly different. As a result, cosmic ray valid events can appear in the previous or following frame from the particle track. These effects are under further investigation.

Although we cannot reduce the unfocused background without eliminating a large amount of signal, we can optimize the signal-to-noise ratio for a given observational science goal. The signal-to-noise ratio is given by

$$SNR = \frac{S_0}{(S_0 + B_0 + \sigma^2 B_0^2)^{1/2}}\,, \tag{1}$$

where S_0 is the number of source counts in the region of interest, B_0 is the number of background counts in

the region of interest, and σ is the fractional systematic uncertainty in the background level ($\sigma \approx 0.05$ for *XMM-Newton* observations, for example). We simulated typical cluster outskirts emission using a diffuse, 2 keV thermal source with surface brightness of 6.2×10^{-16} erg cm^{-2} s^{-1} arcmin^{-2} in the 5–7 keV band, based on Athena Science Requirement 2a-02[‡]. We simulated an accompanying particle background surface brightness using the requirement of 5×10^{-3} cm^{-2} s^{-1} keV^{-1} in the 2–7 keV band. Figure 9 shows how the *SNR* varies with exclusion radius, r_e, for a variety of total exposure times and region of interest sizes. Given all the available

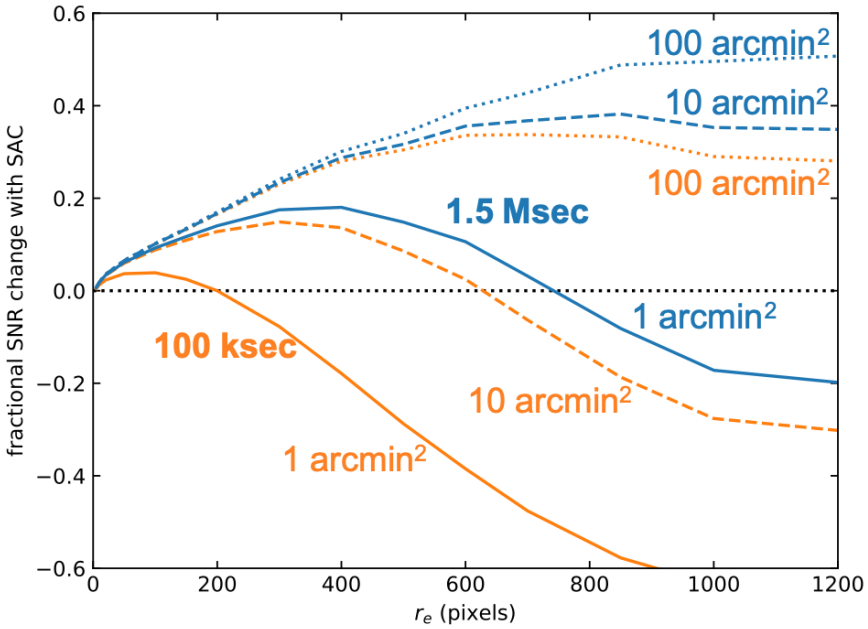

Figure 9. Fractional improvement in SNR using SAC (partial vetoing) as a function of exclusion radius. The model, described in the text, is a diffuse, faint emission source observed for 100 ks (orange) and 1.5 Ms (blue), and searched for extended features of 1 (solid), 10 (dashed), and 100 (dotted) arcmin^2. This includes a systematic background uncertainty of 5%. SAC provides flexible, selective masking out to large exclusion radius that greatly enhances deep exposures of extended sources.

on-board information on the particle track population, the exclusion radius can be adjusted during data analysis to maximize the *SNR*, depending on the particular science goals. This requires the availability on the ground of all of the particle track pixels, which the MPE team believes to be feasible within the WFI telemetry constraints.

4. RAPID SOURCE VARIABILITY

Reverberation mapping has become an important technique for probing the close environments of supermassive black holes: the inner region of the accretion disk, the jet, and the corona that produces intense X-ray continuum emission. X-ray emission from the corona illuminates the accretion disk of infalling material. The additional light travel path to the disk results in a reverberation time lag between correlated variability in the primary continuum emission and in the reprocessed emission from the disk. With sufficient time resolution and effective area, this same technique can be applied to studying the accretion disks of stellar-mass black holes in bright X-ray binaries, in which the characteristic length scales and hence the timescales on which reverberation light travel time delays will be detected are $10^5 \sim 10^6$ times shorter. The technique is illustrated in Fig. 10. If this study can be performed on timescales of $50 - 250\mu$s, the accretion disk around a stellar-mass black hole can be

[‡]Athena Science Requirements Document, SRE-S/ATH/2015/01, rev.2.0.1

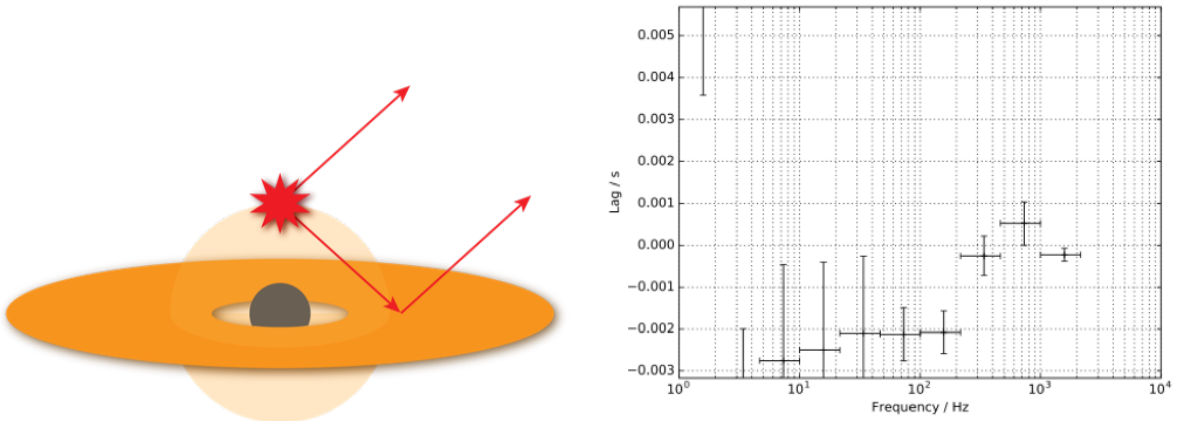

Figure 10. *Left:* Variable X-ray emission is produced in the corona around a black hole. Some of this emission is observed directly on Earth, while some illuminates the accretion disk of infalling material. The irradiated disk reprocesses the emission and its reflection is also observed. Due to the additional light travel time between the X-ray source and the disk, a reverberation response is observed, as correlated variations in the reflected X-rays are delayed with respect to those in the primary continuum. Time delays depend upon the position and geometry of the corona as well as the structure of the disk. The technique can therefore be used to map out the extreme environment around black holes. This has proven extremely successful for supermassive black holes. Application to stellar-mass black holes requires time resolution as short as 50μs, and is a driver for squeezing the best high speed response from the WFI. *Right:* Simulated measurement of the reverberation time delay around a stellar mass black hole in a typical bright X-ray binary that could be measured using the Athena WFI. The simulated time delay is 1000s (negative lags correspond to the detection of reverberation) and is measured as a function of the different frequency Fourier components that make up the slow and fast components of the X-ray variability.

probed to within $1 \sim 5\times$ the size of the event horizon, while the ability to detect a 1000μs delay would probe scales within 20 times the size of the event horizon. This technique requires both a high count rate to sample the rapid X-ray variability, and getting the best time resolution possible from the WFI instrument. If the timing resolution is limited, sampling the X-ray count rate in time bins that are longer than the lag time that is to be measured, the reverberation lag will be systematically overestimated to approximately the bin time.

Because of the "rolling shutter" readout of the DEPFET detectors, detector rows are read out and reset sequentially, which means that the beginning and end integration times for each row are different. If this is not accounted for in data analysis, the inherent resolution of the detection can be significantly smeared out. This is especially true for the fast detector, which is intentionally out of focus so that a point source illuminates many rows of the detector. However, the rolling shutter can be exploited. If sufficient counts are received across enough rows of the detector, measuring the variation in each row independently can improve the effective timing resolution of the detector since each row effectively records the count rate in a different time interval during each readout. We will investigate new algorithms for exploiting the *Athena* WFI readout scheme to maximize the scientific return of high resolution X-ray timing.

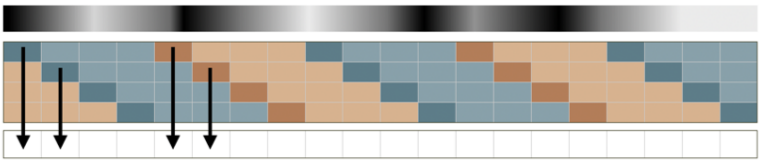

Figure 11. Illustration of the "rolling shutter" readout scheme of the DEPFET detectors. The top shaded bar represents the intrinsic variation in count rate received from the target of the observation. In this example, four detector rows are read out, one after the other, in the dark shaded time intervals. The alternation in color represents the integration period for each row that is recorded in each time bin. The final light curve is represented by the white time bins in the bottom row, with each populated by the row read out at that time, weighted by the point spread function for the fraction of the total flux received by each row.

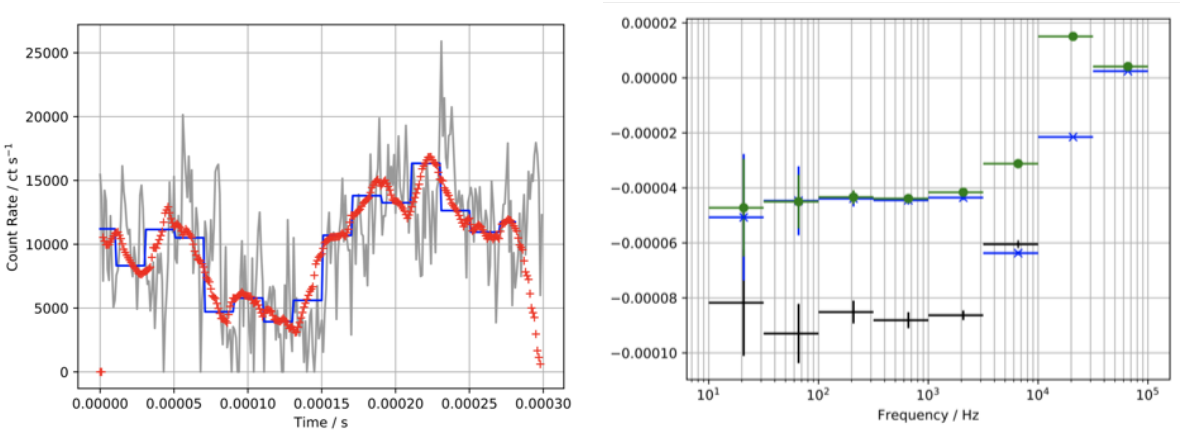

Figure 12. The rolling shutter readout scheme improves the effective timing resolution of the detector. In this example, the target has variability and reverberation time lags on shorter timescales than probed by the total frame time of the detector (where all rows are combined). *Left:* The intrinsic light curve of the target is shown by the black line. When rows are combined into frames, the time resolution is reduced to the binning shown by the blue curve. Exploiting the rolling shutter improves the timing resolution to produce the red curve. *Right:* The time lag as a function of Fourier frequency measured between two light curves. When the time resolution is reduced by reading out frame-by-frame, the time lag is overestimated (black points); however, increasing the timing resolution by using the rolling shutter to read the detector row-by-row recovers the intrinsic 50μs time lag (blue points), further improved at high frequencies by interpolating between readout intervals (green points).

5. FRONT-END ELECTRONICS DEVELOPMENT

Our US team is playing a significant role in the development of the readout electronics for the WFI. While the MPE is responsible for the development of both the front-end electronics and detectors, our team has played a significant collaborative role in the design, testing, and analysis of the readout ASICs, and has provided input to the schematics, simulations and layout of all versions tested to date.

The development of the readout ASICs is an iterative process that proceeds alongside the ongoing development of the DEPFET detectors. The past year saw the production of the most recent ASIC version, VERITAS 2.2, which will be the default readout chip for the DEPFET flight pre-production sensors. Details of the readout ASIC architecture can be found in Herrmann et al.[21]

In order to mitigate implementation risks, especially with regard to aspects that are more challenging to simulate, we elected to manufacture three VERITAS 2.2 variants. The first 'conservative' variant (CV) incorporates minimal changes with respect to the VERITAS 2.1 design, although it includes several important bug fixes. It also adjusts the gain settings and current range to better accommodate the flight (512×512) DEPFETs, which are much larger than the prototype devices used with the VERITAS 2.1 ASIC.

A second, 'moderate' variant (MV) adds input protection clamps to mitigate a potential hazard condition that can cause latchups when the DEPFET sensor supplies overcurrent to the readout ASIC input stage. These clamps act to shunt the excess current to ground. As these clamp structures are located at the most sensitive input node, we decided — despite encouraging simulation results regarding the likely noise impact — not to include this feature in the CV variant. Preliminary tests have shown that the clamp structures are indeed suitable to mitigate the hazard condition with minimal noise impact. Therefore, this variant will become the workhorse ASIC for the upcoming DEPFET preflight production tests.

Our third 'advanced' variant (AV) includes additional design improvements and a new output buffer structure. The latter is designed to drive an ADC input directly, without the need for intermediate buffers and voltage translation.

We are currently assisting MPE with detailed evaluation of the VERITAS 2.2 ASICs. Future steps will include the search for further potential performance improvements, based on the lessons learned from the characterization of these ASICs and the DEPFET preflight production devices. Space qualification remains to be performed, including hazard analysis and mitigation, environmental tests and analysis, lifetime and reliability assessment, and radiation tests and analysis. For long term projects like Athena, process technology availability is always a potential risk. We intend to investigate alternative process technology options for future VERITAS iterations.

ACKNOWLEDGMENTS

We are very grateful for support from NASA grant NNX17AB07G.

REFERENCES

[1] Meidinger, N., Nandra, K., and Plattner, M., "Development of the Wide Field Imager instrument for ATHENA," in [*Proc. SPIE*], *Society of Photo-Optical Instrumentation Engineers (SPIE) Conference Series* **10699**, 106991F (Jul 2018).

[2] Meidinger, N., Barbera, M., Emberger, V., Fürmetz, M., Manhart, M., Müller-Seidlitz, J., Nandra, K., Plattner, M., Rau, A., and Treberspurg, W., "The Wide Field Imager instrument for Athena," in [*Proc. SPIE*], *Society of Photo-Optical Instrumentation Engineers (SPIE) Conference Series* **10397**, 103970V (Aug 2017).

[3] Meidinger, N., Eder, J., Eraerds, T., Nand ra, K., Pietschner, D., Plattner, M., Rau, A., and Strecker, R., "The wide field imager instrument for Athena," in [*Proc. SPIE*], *Society of Photo-Optical Instrumentation Engineers (SPIE) Conference Series* **9905**, 99052A (Jul 2016).

[4] Meidinger, N., Eder, J., Fürmetz, M., Nand ra, K., Pietschner, D., Plattner, M., Rau, A., Reiffers, J., Strecker, R., Barbera, M., Brand, T., and Wilms, J., "Development of the wide field imager for Athena," in [*Proc. SPIE*], *Society of Photo-Optical Instrumentation Engineers (SPIE) Conference Series* **9601**, 96010H (Aug 2015).

[5] Meidinger, N., Nandra, K., Plattner, M., Porro, M., Rau, A., Santangelo, A. E., Tenzer, C., and Wilms, J., "The wide field imager instrument for Athena," in [*Proc. SPIE*], *Society of Photo-Optical Instrumentation Engineers (SPIE) Conference Series* **9144**, 91442J (Jul 2014).

[6] Parodi, G., D'Anca, F., Lo Cicero, U., Sciortino, L., Rataj, M., Polak, S., Pilch, A., Meidinger, N., Dittrich, K., Hartwig, J., Samain, V., Collura, A., Ferruggia Bonura, S., Buttacavoli, A., and Barbera, M., "Structural modelling and mechanical tests supporting the design of the ATHENA X-IFU thermal filters and WFI optical blocking filter," in [*Proc. SPIE*], *Society of Photo-Optical Instrumentation Engineers (SPIE) Conference Series* **10699**, 106994C (Jul 2018).

[7] Plattner, M., Albrecht, S., Bayer, J., Brandt, S., Drumm, P., Hälker, O., Kerschbaum, F., Koch, A., Kuvvetli, I., Meidinger, N., Ott, S., Ottensamer, R., Reiffers, J., Schanz, T., Skup, K., Steller, M., Tenzer, C., and Thomas, C., "WFI electronics and on-board data processing," in [*Proc. SPIE*], *Society of Photo-Optical Instrumentation Engineers (SPIE) Conference Series* **9905**, 99052D (Jul 2016).

[8] Treberspurg, W., Müller-Seidlitz, J., Meidinger, N., Behrens, A., Andritschke, R., Bonholzer, M., Emberger, V., and Hauser, G., "Energy response of ATHENA WFI prototype detectors," in [*Proc. SPIE*], *Society of Photo-Optical Instrumentation Engineers (SPIE) Conference Series* **10699**, 106994F (Jul 2018).

[9] Porro, M., Bianchi, D., De Vita, G., Herrmann, S., Wassatsch, A., Bähr, A., Bergbauer, B., Meidinger, N., Ott, S., and Treis, J., "VERITAS 2.0 a multi-channel readout ASIC suitable for the DEPFET arrays of the WFI for Athena," in [*Proc. SPIE*], *Society of Photo-Optical Instrumentation Engineers (SPIE) Conference Series* **9144**, 91445N (Jul 2014).

[10] Barbera, M., Lo Cicero, U., Sciortino, L., D'Anca, F., Parodi, G., Rataj, M., Polak, S., Pilch, A., Meidinger, N., Sciortino, S., Rauw, G., Brand uardi Raymont, G., Mineo, T., Perinati, E., Giglio, P., Collura, A., Varisco, S., and Cand ia, R., "ATHENA WFI optical blocking filters development status toward the end of the instrument phase-A," in [*Proc. SPIE*], *Society of Photo-Optical Instrumentation Engineers (SPIE) Conference Series* **10699**, 106991K (Jul 2018).

[11] Fürmetz, M., Pietschner, D., and Meidinger, N., "Thermal analysis of the WFI on the ATHENA observatory," in [*Proc. SPIE*], *Society of Photo-Optical Instrumentation Engineers (SPIE) Conference Series* **9905**, 99052E (Jul 2016).

[12] Soderberg, A. M., Berger, E., Page, K. L., Schady, P., Parrent, J., Pooley, D., Wang, X. Y., Ofek, E. O., Cucchiara, A., Rau, A., Waxman, E., Simon, J. D., Bock, D. C. J., Milne, P. A., Page, M. J., Barentine, J. C., Barthelmy, S. D., Beardmore, A. P., Bietenholz, M. F., Brown, P., Burrows, A., Burrows, D. N., Byrngelson, G., Cenko, S. B., Chand ra, P., Cummings, J. R., Fox, D. B., Gal-Yam, A., Gehrels, N., Immler, S., Kasliwal, M., Kong, A. K. H., Krimm, H. A., Kulkarni, S. R., Maccarone, T. J., Mészáros, P., Nakar, E., O'Brien, P. T., Overzier, R. A., de Pasquale, M., Racusin, J., Rea, N., and York, D. G., "An extremely luminous X-ray outburst at the birth of a supernova," *Nature* **453**, 469–474 (May 2008).

[13] CHIME/FRB Collaboration, Amiri, M., Bandura, K., Bhardwaj, M., Boubel, P., Boyce, M. M., Boyle, P. J., . Brar, C., Burhanpurkar, M., Cassanelli, T., Chawla, P., Cliche, J. F., Cubranic, D., Deng, M., Denman, N., Dobbs, M., Fandino, M., Fonseca, E., Gaensler, B. M., Gilbert, A. J., Gill, A., Giri, U., Good, D. C., Halpern, M., Hanna, D. S., Hill, A. S., Hinshaw, G., Höfer, C., Josephy, A., Kaspi, V. M., Landecker, T. L., Lang, D. A., Lin, H. H., Masui, K. W., Mckinven, R., Mena-Parra, J., Merryfield, M., Michilli, D., Milutinovic, N., Moatti, C., Naidu, A., Newburgh, L. B., Ng, C., Patel, C., Pen, U., Pinsonneault-Marotte, T., Pleunis, Z., Rafiei-Ravandi, M., Rahman, M., Ransom, S. M., Renard, A., Scholz, P., Shaw, J. R., Siegel, S. R., Smith, K. M., Stairs, I. H., Tendulkar, S. P., Tretyakov, I., Vanderlinde, K., and Yadav, P., "A second source of repeating fast radio bursts," *Nature* **566**, 235–238 (Jan 2019).

[14] Evans, P. A., Osborne, J. P., Beardmore, A. P., Page, K. L., Willingale, R., Mountford, C. J., Pagani, C., Burrows, D. N., Kennea, J. A., Perri, M., Tagliaferri, G., and Gehrels, N., "1SXPS: A Deep Swift X-Ray Telescope Point Source Catalog with Light Curves and Spectra," *Ap. J. Suppl.* **210**, 8 (Jan 2014).

[15] Pradhan, P., Falcone, A. D., Kennea, J. A., and Burrows, D. N., "Exploring on-board transient detection with the Athena Wide Field Imager," *JATIS, in prep.* (2019).

[16] Dauser, T., Falkner, S., Lorenz, M., Kirsch, C., Peille, P., Cucchetti, E., Schmid, C., Brand, T., Oertel, M., Smith, R., and Wilms, J., "SIXTE – The Generic X-ray Instrument Simulation Toolkit," *arXiv e-prints* , arXiv:1908.00781 (Aug 2019).

[17] von Kienlin, A., Eraerds, T., Bulbul, E., Fioretti, V., Gastaldello, F., Grant, C. E., Hall, D., Holland, A., Keelan, J., Meidinger, N., Molendi, S., Perinati, E., and Rau, A., "Evaluation of the ATHENA/WFI instrumental background," in [*Proc. SPIE*], *Society of Photo-Optical Instrumentation Engineers (SPIE) Conference Series* **10699**, 106991I (Jul 2018).

[18] Tylka, A. J., Adams, J. H., Boberg, P. R., Brownstein, B., Dietrich, W. F., Flueckiger, E. O., Peterson, E. L., Shea, M. A., Smart, D. F., and Smith, E. C., "CREME96: A Revision of the Cosmic Ray Effects on Micro-Electronics Code," *IEEE Transactions on Nuclear Science* **44**, 2150 (December 1997).

[19] Bulbul, E., Kraft, R., Nulsen, P., Freyberg, M., Miller, E. D., Grant, C., Bautz, M. W., Burrows, D. N., Allen, S., Eraerds, T., Fioretti, V., Gasteldello, F., Ghirardini, V., Hall, D., Meidinger, N., Molendi, S., Rau, A., Wilkins, D., and Wilms, J., "Characterizing the Particle-Induced Background of XMM-Newton EPIC-pn: Short and Long Term Variability," *arXiv e-prints* , arXiv:1908.00604 (Aug 2019).

[20] Miller, E., "Characterizing and reducing the particle background on the Athena Wide-Field Imager," *JATIS, in prep.* (2019).

[21] Herrmann, S., Koch, A., Obergassel, S., Treberspurg, W., Bonholzer, M., and Meidinger, N., "VERITAS 2.2: a low noise source follower and drain current readout integrated circuit for the wide field imager on the Athena x-ray satellite," in [*High Energy, Optical, and Infrared Detectors for Astronomy VIII*], *Society of Photo-Optical Instrumentation Engineers (SPIE) Conference Series* **10709**, 1070935 (Jul 2018).